High-Power Growth-Robust InGaAs/InAlAs Terahertz Quantum Cascade Lasers

Journal Article

Author(s):
Deutsch, Christoph; Kainz, Martin A.; Krall, Michael; Brandstetter, Martin; Bachmann, Dominic; Schönhuber, Sebastian; Detz, Hermann; Zederbauer, Tobias; MacFarland, Donald; Andrews, Aaron M.; Schrenk, Werner; Beck, Mattias (ID); Ohtani, Keita; Faist, Jérôme (ID); Strasser, Gottfried; Unterrainer, Karl

ACS **Photonics**

High-Power Growth-Robust InGaAs/InAlAs Terahertz Quantum Cascade Lasers

Christoph Deutsch,[†,§,#] Martin Alexander Kainz,[*,†,§,#] Michael Krall,[†,§] Martin Brandstetter,[†,§] Dominic Bachmann,[†,§] Sebastian Schönhuber,[†,§] Hermann Detz,[§,⊥] Tobias Zederbauer,[‡,§] Donald MacFarland,[‡,§] Aaron Maxwell Andrews,[‡,§] Werner Schrenk,[§] Mattias Beck,[∥] Keita Ohtani,[∥] Jérôme Faist,[∥] Gottfried Strasser,[‡,§] and Karl Unterrainer[†,§]

[†]Photonics Institute, TU Wien, Gußhausstraße 27-29, 1040 Vienna, Austria
[‡]Institute of Solid State Electronics and [§]Center for Micro- and Nanostructures, TU Wien, Floragasse 7, 1040 Vienna, Austria
[∥]Institute for Quantum Electronics, ETH Zurich, Auguste-Piccard-Hof 1, 8093 Zurich, Switzerland
[⊥]Austrian Academy of Sciences, Dr. Ignaz Seipel-Platz 2, 1010 Vienna, Austria

ABSTRACT: We report on high-power terahertz quantum cascade lasers based on low effective electron mass InGaAs/InAlAs semiconductor heterostructures with excellent reproducibility. Growth-related asymmetries in the form of interface roughness and dopant migration play a crucial role in this material system. These bias polarity dependent phenomena are studied using a nominally symmetric active region resulting in a preferential electron transport in the growth direction. A structure based on a three-well optical phonon depletion scheme was optimized for this bias direction. Depending on the sheet doping density, the performance of this structure shows a trade-off between high maximum operating temperature and high output power. While the highest operating temperature of 155 K is observed for a moderate sheet doping density of 2×10^{10} cm^{-2}, the highest peak output power of 151 mW is found for 7.3×10^{10} cm^{-2}. Furthermore, by abutting a hyperhemispherical GaAs lens to a device with the highest doping level a record output power of 587 mW is achieved for double-metal waveguide structures.

KEYWORDS: quantum cascade lasers, terahertz, low effective mass, molecular beam epitaxy, quantized transitions, nanostructures
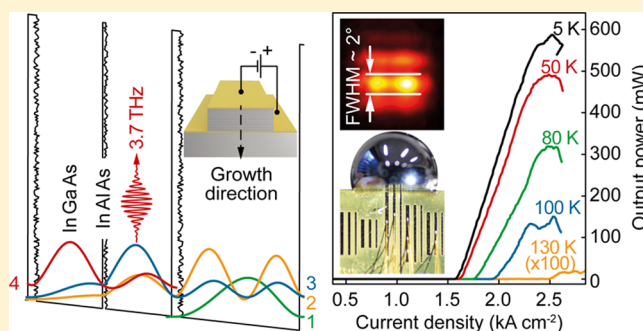
Quantum cascade lasers (QCLs)[1] are based on periodic semiconductor heterostructures and can be designed for a wide range of emission frequencies. For terahertz (THz) operation, achieving a sufficiently large optical gain in the active region becomes more and more challenging with increasing lattice temperature. So far, this has limited the operation of THz QCLs to a maximum heat sink temperature of about 200 K.[2] In addition, the available amount of optical gain also determines the optical output power. Maximum peak output powers up to 1 W with surface plasmon waveguides[3,4] and 145 mW using double-metal waveguides[5] have been obtained so far.

The optical gain that can be achieved in the active region is apart from the quantum design fundamentally related to the material parameters associated with the semiconductor heterostructure. Most notably, it scales inversely with the effective mass of the charge carriers, which directly favors material systems with a low effective electron mass.[6]

THz QCLs have been most commonly realized using the GaAs/Al$_x$Ga$_{1-x}$As material system,[7] for which lattice matching can be obtained over a wide range of barrier compositions, allowing the adjustment of the barrier height. Alternative candidates with lower effective electron mass include InGaAs/

InAl(Ga)As,[8,9] InGaAs/GaAsSb,[10] and InAs/AlAsSb[11] with compositions lattice matched to InP or InAs, respectively. The latter is very promising due to the lowest effective mass; however only lasing in magnetic fields has been achieved so far. A more mature choice is the InGaAs/InAlAs material combination, which is well developed and already commonly used for mid-infrared QCL devices. Nevertheless, there has been a reluctance to use it for THz QCLs due to the relatively large conduction band offset (CBO). This results in very thin barriers on the order of a single monolayer, creating high requirements on the epitaxial growth.[12] Therefore, InGaAs/GaAsSb[10,13] and InGaAs/InAlGaAs[9,14,15] material combinations with lower barriers resulting in maximum operating temperatures of 142 and 149 K, respectively, have been studied. On the other hand, recent investigations indicate that high barriers can actually be beneficial in terms of reduced leakage currents.[16,17]

Although THz QCLs have a unipolar carrier transport, which makes it possible to realize symmetric active regions, dopant

migration and interface roughness strongly influence their current direction dependent performance. In a previous study[18] we have investigated dopant migration effects of a symmetric GaAs/AlGaAs structure, which performs better for positive bias direction (electron flow against growth direction) because for negative bias direction the doping migration region extends into the lasing transition, resulting in a reduction of the lifetime of the upper laser level. Compensation for dopant migration results in a lower current density and better performance for the negative bias direction. The influence of interface roughness scattering was studied in the InGaAs/GaAsSb/InP material system,[19] which shows a pronounced interface asymmetry. For positive bias (electron flow against growth direction), the electrons are incident on the rougher interface, which causes a stronger interface roughness scattering. Thus, higher optical output power and lower threshold current density are obtained for negative bias.

So far, the best InGaAs/InAlAs THz QCLs were based on a (four-well) bound-to-continuum design[20] and showed lasing only up to 122 K. However, for GaAs/AlGaAs-based THz QCLs, the best temperature performance has been achieved with a three-well resonant phonon extraction design.[2]

Here, we show that by combining an InGaAs/InAlAs structure, with its low effective electron mass, and a three-well resonant phonon extraction design, high output power as well as good temperature performance can be achieved when growth asymmetries are taken into account and are compensated.

■ INFLUENCE OF GROWTH-RELATED ASYMMETRIES

As a first step, a symmetric structure was designed to study the bias polarity dependence to get a better knowledge on dopant migration[18] and interface roughness[19] effects for this material system. Both growth asymmetries strongly influence the performance of GaAs/AlGaAs[18] and InGaAs/GaAsSb[19] THz QCLs. Thus, it is important to study these effects for any other material system as well. Recent results from direct interface roughness measurements of InGaAs/InAlAs heterojunctions grown by MOCVD show that InGaAs-on-InAlAs interfaces are rougher and more strongly correlated than InAlAs-on-InGaAs ones.[21] Therefore, we expect also a favored operating direction with respect to the growth direction, as recently shown for symmetric InGaAs/InAlAs mid-infrared QCL structures.[22]

The used symmetric quantum cascade structure is based on a three-well active region design,[23] consisting of two tunnel-coupled wells for the lasing states and one well for the carrier injection and a fast resonant phonon depopulation. The layer sequence of the structure in nanometers for a single period was **1.8**/13.3/**0.6**/13.3/**1.8**/9/_6_/9 with the $In_{0.52}Al_{0.48}As$ barriers indicated in bold letters and $In_{0.53}Ga_{0.47}As$ wells, whereas the doped region is underlined. The respective compositions are lattice matched to InP. The electronic band structures depicting the energy levels and the squared wave functions at a design field of +10 kV/cm for positive (a) and −10 kV/cm for negative (b) top bias polarity are shown in Figure 1.

The expected interface roughness is indicated with the zigzag pattern. The thinnest barrier of the layer structure essentially determines the oscillator strength of the optical transition, while the injector and extractor coupling strengths are defined by the respective thickness of the two other barriers. Efficient extraction of the lower laser level is achieved by resonant longitudinal optical (LO) phonon emission in the widest well of the structure. The dashed line in Figure 1c represents the
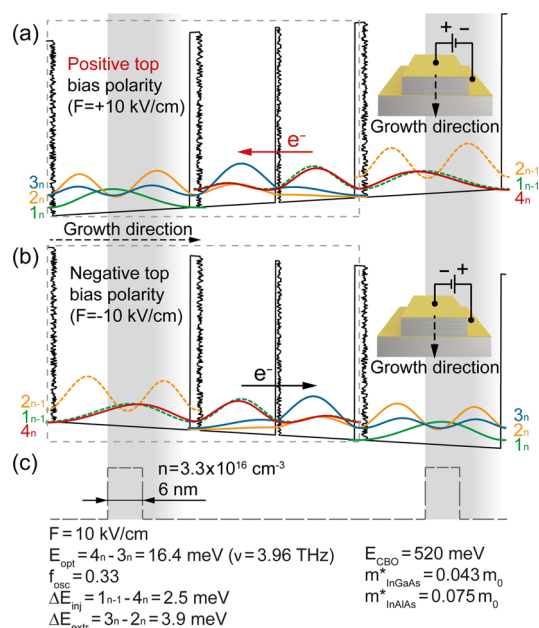

Figure 1. Band structure of the symmetric three-well resonant phonon quantum cascade design for an applied electric field F of 10 kV/cm. The framed region indicates a single cascade, which is repeated 222 times. The relevant energy levels (squared wave functions) associated with period n (1_n–4_n) are plotted in color. Growth-related interface roughness is indicated as zigzag lines. (a) Positive top bias polarity with electron flow against the growth direction and (b) negative top bias polarity with electron flow in the growth direction. (c) The gray dashed line marks the location of the dopants, whereas the blurred regions illustrate dopant migration. The optical transition energy, E_{opt}, the oscillator strength, f_{osc}, and the injector (extractor) coupling strength, ΔE_{inj} (ΔE_{extr}), are listed in the figure.

nominal doping profile, and the shaded regions indicate the assumed dopant migration. The nominal width of 6 nm with a doping density of 3.3×10^{16} cm^{-3} results in a sheet doping density n_s of 2×10^{10} cm^{-2}. The periodic semiconductor heterostructure of the active region was grown using a Veeco GEN II molecular beam epitaxy (MBE) system. The layer sequence of a single period was repeated 222 times with a 50 nm (100 nm) thick highly doped contact layer on the bottom (top), resulting in a total thickness of 12.2 μm. By X-ray diffraction analysis a deviation of +2% from the nominal period length ($\Delta L/L$) was determined.

From this active region standard laser ridges with a double-metal (Au−Au) waveguide geometry were fabricated.[24] The laser ridges were defined by depositing the top metal waveguide layer (Ti/Au) together with a Ni etch mask onto the active region. A reactive ion etching process (ICP-RIE) based on a SiCl$_4$/Ar chemistry was employed to create ridges with steep sidewalls.

The devices were indium soldered to a copper plate and mounted on the cold finger of a liquid helium continuous-flow cryostat for controlling the heat sink temperature. A series of devices was characterized by light−current−voltage (LIV) measurements. The emitted THz radiation was collected by a parabolic mirror and analyzed using a Fourier-transform infrared (FTIR) spectrometer (Bruker Vertex 80) with an integrated DTGS far-infrared detector. The measurements of the optical output power were performed using a thermopile detector mounted inside the vacuum chamber of the cryostat in close vicinity to the laser facet.

Figure 2 shows the LIV characteristics for negative and positive bias voltage, with electron flow in and against the
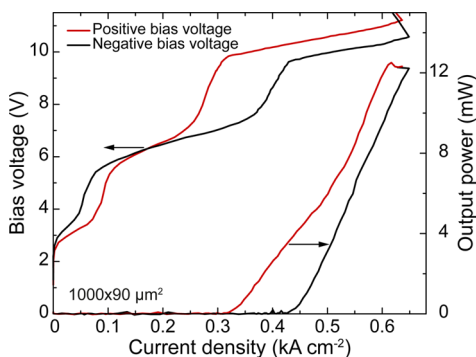
Figure 2. Comparison of the two operating directions of a symmetric active region structure with centered doping profile. The light−current−voltage characteristics were measured for positive and negative top bias voltage. The devices were operated in pulsed mode (200 ns, 200 kHz) at a temperature of 5 K.

growth direction, respectively. For the positive bias direction, the threshold current density is 0.31 kA/cm^2, whereas for the negative one it is 0.44 kA/cm^2. Such an asymmetry was also observed for GaAs/AlGaAs THz QCLs, where dopant migration is the dominant cause for the asymmetry.[18] At low bias voltage two tunnel resonances occur. The first one at 3.3 V belongs to a parasitic alignment over two periods ($1n-2n+2$), whereas the second one at 6.4 V is the tunnel resonance for one period ($1n-2n+1$). The calculated wave functions for the first resonance are more located in the thinner wells and therefore more strongly influenced by the interfaces, whereas for the resonance at higher bias the wave functions are mainly located in the widest well. The experimentally observed asymmetry of these two resonances confirms that the first resonance is more influenced by interface roughness, whereas the second one by doping migration. On average, the peak output power P_{peak} for positive polarity is 15% higher than for negative polarity at a heat sink temperature of 5 K, but it drops much faster with elevated temperatures. The slope efficiency dP/dI for the negative operation direction is 26% higher than for the positive one. This is a strong indication for a higher internal quantum efficiency for negative bias polarity. Moreover, for negative polarity the maximum operating temperature T_{max}^- of 144 K is higher compared to that for a positive polarity T_{max}^+ of 131 K. Overall, negative polarity showed a better lasing performance despite the adverse effects of increased impurity scattering and consequently a higher threshold current density. We conclude that the observed polarity-dependent effects are very likely attributed to interface roughness asymmetry of the barriers as observed for InGaAs/GaAsSb THz QCLs.[19] For the InGaAs/InAlAs material system a strong influence on the interface asymmetry is not surprising at all since the interface roughness scattering rate scales quadratically with the CBO[19] and is hence very high compared to that of GaAs/Al$_{0.15}$Ga$_{0.85}$As.

■ HIGH-PERFORMANCE ASYMMETRIC DEVICES

In the second part, we focused on optimized asymmetric devices that were operated in the negative bias direction. In these lasers, the electron transport was along the growth direction, which results in a longer upper level lifetime compared to the opposite transport direction.[19] In addition,

the doping profile was shifted against the growth direction to compensate for dopant migration and to reduce impurity scattering of the upper lasing level. Furthermore, the influence of doping concentration on the optical gain and the maximum operating temperature was studied by comparing samples with an identical quantum cascade design, but with different doping concentrations.

The layer sequence of the optimized quantum cascade design in nanometers for a single period was **1.8**/13.3/**0.6**/13.3/**1.5**/6/18 with the same labeling as before. The extractor barrier was reduced from 1.8 nm to 1.5 nm to increase the extractor coupling strength. The doping was placed in the first 6 nm of the phonon well. This shift from the center was chosen in order to reduce deteriorating effects of dopant migration and the resulting impurity scattering.[18] As for the symmetric structure, the layer sequence of a single period was always repeated 222 times. To study the influence of doping concentration in the active region, the doping density (n_s) was varied between 1×10^{10} and 7.3×10^{10} cm^{-2}. The samples were grown using three different MBE systems in four different growth campaigns at two different laboratories to study the reproducibility of the design. An overview of the grown samples is listed in Table 1, which also gives the deviation of the period length $\Delta L/L$ obtained by X-ray diffraction analysis.

Table 1. Overview of Asymmetric THz QCL Samples Studied and Compared in This Work^a

| sample ID	MBE system	sheet doping density (10^{10} cm^{-2})	$\Delta L/L$ (%)
A	Riber Compact 21	1	−0.7
B	Riber Compact 21	2	+2.7
C	VG V80H	2	+2.4
D	Riber Compact 21	4	+2.0
E	Veeco GEN II	7.3	+1.8

^{a}The sheet doping density n_s is given in units of 10^{10} cm^{-2}. In addition, the deviation of the period length ΔL from its nominal value L is given.

A series of devices with double-metal (Au−Au) waveguide geometry was fabricated from each active region and characterized as described above for the symmetric active region devices. Typical sizes for the laser ridges varied between 1000×60 and 2000×120 μm^2 with either cleaved or etched facets.[25]

Figure 3 shows the LIV measurements for two typical devices with equal sheet doping density of 2×10^{10} cm^{-2}. They were fabricated from the active region samples B and C and processed using the same processing parameters. The devices were operated in pulsed mode (500 ns, 10 kHz). The threshold current density J_{th} at 5 K is around 0.4 kA/cm^2 and agrees well for both active regions. This is also the case for the alignment fields and the onset of the negative differential resistance (NDR) region (around 10.7 V). Characteristic emission spectra at low temperatures are shown in the insets of Figure 3 with the dominant lasing modes around 3.7 THz. The maximum operating temperature was also very similar to lasing emission up to 155 and 154 K for samples B and C, respectively. The close agreement of the two samples shows the reproducibility of these results and is also an excellent proof of the growth robustness of the structure.

Besides the layer structure of the active region, the dopant concentration and position play a critical role for the
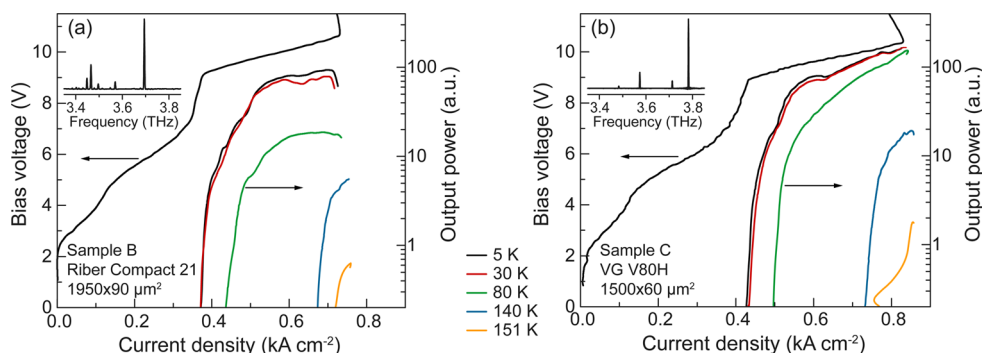
Figure 3. Light−current−voltage characteristics of typical devices fabricated from two nominally identical active regions with equal sheet doping density (2×10^{10} cm^{-2}). The current−voltage measurement is given for a heat sink temperature of 5 K, and the optical power measurements up to a heat sink temperature of 151 K. The insets show the measured emission spectra of the respective device for the operating point of maximum output power at 5 K.

performance of THz QCLs. Due to the rather low doping concentrations in THz QCLs, effects on the band structure (band bending) are very limited. Previous investigations into the influence of doping on the performance of GaAs/AlGaAs THz QCLs have shown an approximately linear dependence of the threshold current density on the doping level.[26,27] However, the amount of dopants influences not only the current density but even more importantly the optical gain. On one hand, a larger amount of carriers increases the potential population inversion, but on the other hand, it also reduces the nonradiative lifetime, due to increased impurity scattering.[28] In terms of waveguide losses, higher doping densities do not limit the performance of the quantum cascade device, due to very small free-carrier absorption coefficients at low temperatures.[29]

Figure 4a illustrates the impact of different doping on the threshold current density (J_{th}) and the current density at maximum intensity (J_{max}). Similar to previous investigations, the threshold current density scales in this range linearly with the doping density.[26] This results from the fact that it is mainly determined by the electrical alignment and therefore by the applied bias.

The output power at a heat sink temperature of 5 K was measured for a series of devices using low duty cycles (0.5%) in order to prohibit an excessive heating of the active region. In general, the output power increases with doping concentration, as illustrated in Figure 4b. The highest peak output power of 151 mW was achieved from a device with a sheet doping density of 7.3×10^{10} cm^{-2} (sample E). These results indicate that at low temperatures (5 K) the increase in optical gain, due to a larger number of free carriers, outbalances the increase in scattering resulting from the larger number of impurities. The inset in Figure 4b shows the output power as a function of operating temperature for several devices. By comparing the wall-plug efficiency for the four dopant concentrations, the highest value occurs for a sheet doping density of 4×10^{10} cm^{-2} with a maximum value of 0.47%.

Figure 4c compares the maximum operating temperature in pulsed mode of the devices fabricated from each active region listed in Table 1. The best temperature performance was observed for a sheet doping density of 2×10^{10} cm^{-2} with a maximum operating temperature of 155 K for sample B. This shows that at elevated temperatures for lower doping concentrations the smaller number of carriers reduces the optical gain, whereas for higher doping levels the decrease in
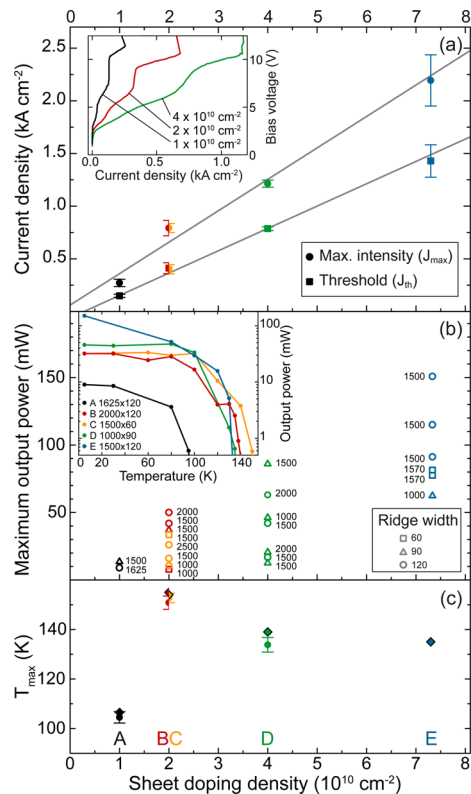

Figure 4. Influence of the doping density on the performance of the active region. (a) The average threshold current density at 5 K of devices from various samples scales linearly with doping concentration. The gray lines indicate a linear fit to the data points for the threshold current density and the current density at the maximum intensity, respectively. The inset shows the current−voltage characterization for the three lowest doping densities. (b) The peak output power in pulsed operation at 5 K is highest (151 mW) for the largest studied doping concentration. Different ridge sizes (in μm) are labeled with a square, triangle, or circle for the width, whereas the length is written next to the marker. The inset shows the output power against the operating temperature for several devices. (c) Average maximum operating temperature in pulsed operation. The black framed squares on top depict the best device for each sample. The temperature peaks for a sheet doping density of 2×10^{10} cm^{-2} at 155 and 154 K for samples B and C, respectively.

optical gain due to reduced lifetimes exceeds the increase of optical gain resulting from the larger amount of carriers.

LENS COUPLING FOR OUTPUT POWER ENHANCEMENT

To improve the out-coupling efficiency as well as the collection efficiency, a hyperhemispherical GaAs lens with a diameter of 3 mm and a total length of 2 mm was mounted at the cleaved facet of a QCL ridge. The inset of Figure 5 shows a photograph
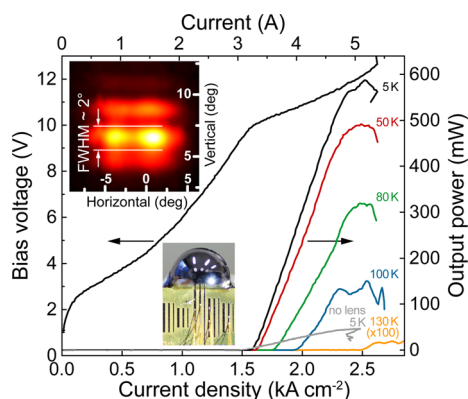
Figure 5. Peak output power measurement with an attached hyperhemispherical GaAs lens at different heat sink temperatures. The used laser ridge has a length of 1830 μm and a width of 112 μm with a sheet doping density of 7.3×10^{10} cm^{-2} (sample E). In addition the optical output power without a lens is shown for a temperature of 5 K. The two insets show a photograph of the mounted lens on the measured device and the far field measured at a distance of 13 cm.

of the device with the mounted GaAs lens. The sample was aligned and indium soldered to a copper plate to have the output facet aligned with the edge of the copper carrier. Figure 5 shows the LIV measurements with the lens attached to a laser ridge of sample E. The device has a length of 1830 μm and a width of 112 μm. In pulsed operation (500 ns, 1 kHz) and at a temperature of 5 K a peak output power of 587 mW was achieved with a wall-plug efficiency of 0.98%. At 80 K the device still delivers an output power of 320 mW. Compared to the measurement without a lens, at a temperature of 5 K the output power of this device was substantially increased from 46 mW by a factor of 13. By extrapolating the wall-plug efficiency of this device to the best wall-plug efficiency for a sheet doping density of 4×10^{10} cm^{-2}, a value of 1.3% can be expected.

To determine the beam shape with the attached lens, the far field was measured using a single pixel detector, which was scanned at a distance of 13 cm in front of the device. The inset of Figure 5 shows a very narrow beam profile with a full width at half-maximum (fwhm) of 2° and verifies the high directivity of this lens-coupled configuration.

CONCLUSION

We were able to considerably enhance the performance of low effective electron mass InGaAs/InAlAs THz QCLs by taking into account the influence of semiconductor interfaces and electrical doping. In particular, we have studied the effects of interface roughness, dopant migration, and sheet doping density. The investigation of a nominally symmetric active region indicated important growth-related asymmetries that have to be carefully considered in the device design. These results led to an optimized, asymmetric three-well resonant phonon depletion design with an excellent growth robustness. With this structure we obtained the highest temperature operation of an InGaAs-based THz QCL and exceeded the

previous power record[5] for a double-metal waveguide device by a factor of 4. Particularly at low temperatures, the high optical gain due to the low effective electron mass results in a large output power. The investigation also showed that the output power can be considerably increased with higher doping, while a lower doping level yields the best temperature performance. Attaching a GaAs lens to the output facet of the QCL ridge results in an additional increase of the THz output power as well as in a narrow beam profile, making this lens-coupled configuration particularly suitable for THz imaging applications.

The presented work provides important insights and indicates potential directions for continuing improvements of the InGaAs/InAlAs-based quantum cascade design. While for GaAs/AlGaAs thorough optimizations of common design schemes have already been performed theoretically as well as experimentally,[30] this is something that will require a separate analysis for the InGaAs/InAlAs material system. The results presented in this work indicate that the optimum design parameters considerably depend on the underlying material system. Important design parameters that have to be studied in more detail are the coupling strengths. Another aspect is the impact of the relative alignment between the injection and extraction mechanism. We expect that with a further investigation and optimization of InGaAs/InAlAs quantum cascade designs an even better temperature performance and output power can be achieved.

Our results demonstrate quite impressively that lower effective mass materials can significantly advance THz QCLs. We have shown that InGaAs QCLs due to the increase of the matrix element produce larger output power compared to GaAs QCLs, which have been studied and optimized for several years. To achieve this result, only two small design changes were required. These changes were indicated by bias direction studies, which also provided new insights into the influence of interface roughness of these structures. The excellent transport characteristics combined with the large gain values of these structures also open up the route to multiwavelength or ultrabroadband devices for frequency combs or mode-locking.

AUTHOR INFORMATION

Corresponding Author
*E-mail (M. A. Kainz): martin.kainz@tuwien.ac.at.

ORCID ⓘ
Martin Alexander Kainz: 0000-0002-6504-5862
Hermann Detz: 0000-0002-4167-3653
Aaron Maxwell Andrews: 0000-0002-5790-2588
Keita Ohtani: 0000-0001-6960-1689

Author Contributions
#C. Deutsch and M. A. Kainz contributed equally to this work.

Notes
The authors declare no competing financial interest.

REFERENCES

(1) Faist, J.; Capasso, F.; Sivco, D. L.; Sirtori, C.; Hutchinson, A. L.; Cho, A. Y. Quantum Cascade Laser. *Science* **1994**, *264*, 553−556.

(2) Fathololoumi, S.; Dupont, E.; Chan, C. W. I.; Wasilewski, Z. R.; Laframboise, S. R.; Ban, D.; Mátyás, A.; Jirauschek, C.; Hu, Q.; Liu, H. C. Terahertz Quantum Cascade Lasers Operating up to ∼ 200 K with Optimized Oscillator Strength and Improved Injection Tunneling. *Opt. Express* **2012**, *20*, 3866−3876.

(3) Brandstetter, M.; Deutsch, C.; Krall, M.; Detz, H.; MacFarland, D. C.; Zederbauer, T.; Andrews, A. M.; Schrenk, W.; Strasser, G.; Unterrainer, K. High Power Terahertz Quantum Cascade Lasers with Symmetric Wafer Bonded Active Regions. *Appl. Phys. Lett.* **2013**, *103*, 171113.

(4) Li, L.; Chen, L.; Zhu, J.; Freeman, J.; Dean, P.; Valavanis, A.; Davies, A. G.; Linfield, E. H. Terahertz Quantum Cascade Lasers with > 1 W Output Powers. *Electron. Lett.* **2014**, *50*, 309−311.

(5) Lee, A. W. M.; Qin, Q.; Kumar, S.; Williams, B. S.; Hu, Q.; Reno, J. L. High-Power and High-Temperature THz Quantum-Cascade Lasers Based on Lens-Coupled Metal-Metal Waveguides. *Opt. Lett.* **2007**, *32*, 2840.

(6) Benveniste, E.; Vasanelli, A.; Delteil, A.; Devenson, J.; Teissier, R.; Baranov, A.; Andrews, A. M.; Strasser, G.; Sagnes, I.; Sirtori, C. Influence of the Material Parameters on Quantum Cascade Devices. *Appl. Phys. Lett.* **2008**, *93*, 131108.

(7) Köhler, R.; Tredicucci, A.; Beltram, F.; Beere, H. E.; Linfield, E. H.; Davies, A. G.; Ritchie, D. A.; Iotti, R. C.; Rossi, F. Terahertz Semiconductor-Heterostructure Laser. *Nature* **2002**, *417*, 156−159.

(8) Ajili, L.; Scalari, G.; Hoyler, N.; Giovannini, M.; Faist, J. InGaAs−AlInAs/InP Terahertz Quantum Cascade Laser. *Appl. Phys. Lett.* **2005**, *87*, 141107.

(9) Ohtani, K.; Beck, M.; Scalari, G.; Faist, J. Terahertz Quantum Cascade Lasers Based on Quaternary AlInGaAs Barriers. *Appl. Phys. Lett.* **2013**, *103*, 041103.

(10) Deutsch, C.; Benz, A.; Detz, H.; Klang, P.; Nobile, M.; Andrews, A. M.; Schrenk, W.; Kubis, T.; Vogl, P.; Strasser, G.; Unterrainer, K. Terahertz Quantum Cascade Lasers Based on Type II InGaAs/GaAsSb/InP. *Appl. Phys. Lett.* **2010**, *97*, 261110.

(11) Brandstetter, M.; Kainz, M. A.; Zederbauer, T.; Krall, M.; Schönhuber, S.; Detz, H.; Schrenk, W.; Andrews, A. M.; Strasser, G.; Unterrainer, K. InAs Based Terahertz Quantum Cascade Lasers. *Appl. Phys. Lett.* **2016**, *108*, 011109.

(12) Fischer, M.; Scalari, G.; Walther, C.; Faist, J. Terahertz Quantum Cascade Lasers Based on $In_{0.53}Ga_{0.47}As/In_{0.52}Al_{0.48}As/InP$. *J. Cryst. Growth* **2009**, *311*, 1939−1943.

(13) Deutsch, C.; Krall, M.; Brandstetter, M.; Detz, H.; Andrews, A. M.; Klang, P.; Schrenk, W.; Strasser, G.; Unterrainer, K. High Performance InGaAs/GaAsSb Terahertz Quantum Cascade Lasers Operating up to 142 K. *Appl. Phys. Lett.* **2012**, *101*, 211117.

(14) Valmorra, F.; Scalari, G.; Ohtani, K.; Beck, M.; Faist, J. InGaAs/AlInGaAs THz Quantum Cascade Lasers Operating up to 195 K in Strong Magnetic Field. *New J. Phys.* **2015**, *17*, 023050.

(15) Ohtani, K.; Beck, M.; Faist, J. Strain-Compensated InGaAs Terahertz Quantum Cascade Lasers. *ACS Photonics* **2016**, *3*, 2297.

(16) Albo, A.; Hu, Q. Carrier Leakage into the Continuum in Diagonal GaAs/Al0.15GaAs Terahertz Quantum Cascade Lasers. *Appl. Phys. Lett.* **2015**, *107*, 241101.

(17) Schrottke, L.; Lü, X.; Rozas, G.; Biermann, K.; Grahn, H. T. Terahertz GaAs/AlAs Quantum-Cascade Lasers. *Appl. Phys. Lett.* **2016**, *108*, 102102.

(18) Deutsch, C.; Detz, H.; Krall, M.; Brandstetter, M.; Zederbauer, T.; Andrews, A. M.; Schrenk, W.; Strasser, G.; Unterrainer, K. Dopant Migration Effects in Terahertz Quantum Cascade Lasers. *Appl. Phys. Lett.* **2013**, *102*, 201102.

(19) Deutsch, C.; Detz, H.; Zederbauer, T.; Andrews, A. M.; Klang, P.; Kubis, T.; Klimeck, G.; Schuster, M. E.; Schrenk, W.; Strasser, G.; Unterrainer, K. Probing Scattering Mechanisms with Symmetric Quantum Cascade Lasers. *Opt. Express* **2013**, *21*, 7209.

(20) Fischer, M.; Scalari, G.; Celebi, K.; Amanti, M.; Walther, C.; Beck, M.; Faist, J. Scattering Processes in Terahertz InGaAs/InAlAs Quantum Cascade Lasers. *Appl. Phys. Lett.* **2010**, *97*, 221114.

(21) Lopez, F.; Wood, M. R.; Weimer, M.; Gmachl, C. F.; Caneau, C. G. *Direct Measurements of Interface Roughness in QCL Materials Grown by MOCVD*; International Conference on Intersubband Transitions in Quantum Wells, Lake George, Bolton Landing, New York, 2013.

(22) Bouzi, P. M.; Chiu, Y.; Deutsch, C.; Dikmelik, Y.; Song, Y.; Tokranov, V.; Oktyabrsky, S.; Gmachl, C. Importance of Growth Direction in Mid-Infrared Quantum Cascade Lasers. *J. Appl. Phys.* **2014**, *116*, 034504.

(23) Luo, H.; Laframboise, S. R.; Wasilewski, Z. R.; Aers, G. C.; Liu, H. C.; Cao, J. C. Terahertz Quantum-Cascade Lasers Based on a Three-Well Active Module. *Appl. Phys. Lett.* **2007**, *90*, 041112.

(24) Williams, B. S.; Kumar, S.; Callebaut, H.; Hu, Q.; Reno, J. L. Terahertz Quantum-Cascade Laser at $\lambda \approx 100$ μm Using Metal Waveguide for Mode Confinement. *Appl. Phys. Lett.* **2003**, *83*, 2124.

(25) Brandstetter, M.; Krall, M.; Deutsch, C.; Detz, H.; Andrews, A. M.; Schrenk, W.; Strasser, G.; Unterrainer, K. Influence of the Facet Type on the Performance of Terahertz Quantum Cascade Lasers with Double-Metal Waveguides. *Appl. Phys. Lett.* **2013**, *102*, 231121.

(26) Benz, A.; Fasching, G.; Andrews, A. M.; Martl, M.; Unterrainer, K.; Roch, T.; Schrenk, W.; Golka, S.; Strasser, G. Influence of Doping on the Performance of Terahertz Quantum-Cascade Lasers. *Appl. Phys. Lett.* **2007**, *90*, 101107.

(27) Amanti, M. I.; Scalari, G.; Terazzi, R.; Fischer, M.; Beck, M.; Faist, J.; Rudra, A.; Gallo, P.; Kapon, E. Bound-to-Continuum Terahertz Quantum Cascade Laser with a Single-Quantum-Well Phonon Extraction/Injection Stage. *New J. Phys.* **2009**, *11*, 125022.

(28) Grange, T. Contrasting Influence of Charged Impurities on Transport and Gain in Terahertz Quantum Cascade Lasers. *Phys. Rev. B: Condens. Matter Mater. Phys.* **2015**, *92*, 241306.

(29) Carosella, F.; Ndebeka-Bandou, C.; Ferreira, R.; Dupont, E.; Unterrainer, K.; Strasser, G.; Wacker, A.; Bastard, G. Free-Carrier Absorption in Quantum Cascade Structures. *Phys. Rev. B: Condens. Matter Mater. Phys.* **2012**, *85*, 085310.

(30) Scalari, G.; Walther, C.; Fischer, M.; Terazzi, R.; Beere, H.; Ritchie, D.; Faist, J. THz and Sub-THz Quantum Cascade Lasers. *Laser Photonics Rev.* **2009**, *3*, 45−66.